Microstructural Response During Isothermal and Isobaric Loading of a Precipitation-Strengthened Ni-29.7Ti-20Hf High-Temperature Shape Memory Alloy

O. BENAFAN, R.D. NOEBE, S.A. PADULA II, and R. VAIDYANATHAN

A stable Ni-rich Ni-29.7Ti-20Hf (at. pct) shape memory alloy, with relatively high transformation temperatures, was shown to exhibit promising properties at lower raw material cost when compared to typical NiTi-X (X = Pt, Pd, Au) high-temperature shape memory alloys (HTSMAs). The excellent dimensional stability and high work output for this alloy were attributed to a coherent, nanometer size precipitate phase observed using transmission electron microscopy. To establish an understanding of the role of these precipitates on the microstructure and ensuing stability of the NiTiHf alloy, a detailed study of the micromechanical and microstructural behaviors was performed. *In-situ* neutron diffraction at stress and temperature was used to obtain quantitative information on phase-specific internal strain, texture, and phase volume fractions during both isothermal and isobaric testing of the alloy. During isothermal testing, the alloy exhibited low isothermal strains due to limited detwinning, consistent with direct measurements of the bulk texture through neutron diffraction. This limited detwinning was attributed to the pinning of twin and variant boundaries by the dispersion of fine precipitates. During isobaric thermal cycling at 400 MPa, the high work output and near-perfect dimensional stability was attributed to the presence of the precipitates that act as homogeneous sources for the nucleation of martensite throughout the material, while providing resistance to irrecoverable processes such as plastic deformation.

DOI: 10.1007/s11661-012-1297-z

I. INTRODUCTION

THE unique property of shape memory alloys (SMAs) to recover their original undeformed shape when heated has made them useful multifunctional materials for the development of adaptive engineering structures. This distinctive ability is a result of a displacive, solid-to-solid martensitic phase transformation between a high-temperature, higher symmetry austenite phase (cubic B2), and a lower temperature, lower symmetry martensite phase (*e.g.*, orthorhombic B19 or B33, monoclinic B19′, trigonal *R*-phase, *etc.*). Through this martensitic transformation, SMAs can generate recoverable shape changes of several percent strain even when opposed by large stresses (*e.g.*, up to 500 MPa), resulting in high work output that is competitive with, or superior to, conventional hydraulic, pneumatic, or electromagnetic actuators.[1,2] In addition, SMAs can function as both the sensor and actuator in a single mechanism, reducing engineering complexities. Hence, SMAs are a promising alternative to conventional actuators in aerospace and automotive applications.[3–6]

However, broad commercial success of SMA actuators has remained elusive. This is largely attributed to the fact that commercially available SMAs are primarily limited to binary NiTi alloys that generally exhibit phase transformations at temperatures from slightly below room temperature to around 373 K (100 °C),[7] severely restricting the environment in which they can be used. Furthermore, binary NiTi alloys can be dimensionally unstable, displaying significant irrecoverable strains during repeated thermomechanical cycling.[8,9] Various methods were proposed to address both limitations, *i.e.*, the relatively low transformation temperatures and poor dimensional stability often associated with many SMA systems. The addition of Pt, Pd, Zr, or Hf to binary NiTi was shown to increase transformation temperatures.[10] However, none of these systems are without disadvantages, including the rising cost of precious metals, limited transformation strains, and the aforementioned issues associated with dimensional stability. In an attempt to improve the shape memory behavior of these high-temperature systems, various approaches such as solid-solution strengthening,[11,12] thermomechanical cycling/training,[13–15] severe plastic deformation processing,[15–18] and precipitation strengthening[19,20] were

O. BENAFAN, formerly Graduate Student, with the Advanced Materials Processing and Analysis Center (AMPAC), Mechanical, Materials and Aerospace Engineering Department, University of Central Florida, Orlando, FL 32816, and is now Materials Research Engineer, with the NASA Glenn Research Center, Structures and Materials Division, Cleveland, OH 44135. R.D. NOEBE and S.A. PADULA II, Materials Research Engineers, are with the NASA Glenn Research Center, Structures and Materials Division. R. VAIDYANATHAN, Associate Professor, is with the Advanced Materials Processing and Analysis Center (AMPAC), Mechanical, Materials and Aerospace Engineering Department, University of Central Florida. Contact e-mail: raj@ucf.edu

Manuscript submitted August 25, 2011.
Article published online September 26, 2012

attempted with various degrees of success. In most cases, however, the emphasis was on mere demonstration of high-temperature shape memory alloy (HTSMA) behavior with little effort to develop HTSMAs with optimal work output and dimensional stability. Similar techniques have also been applied to ferromagnetic SMAs in an attempt to improve their mechanical and functional properties.[21,22]

Little can be done to address the cost of raw materials other than to focus on systems such as NiTiZr and NiTiHf that do not contain precious metals. Reports on NiTiHf HTSMAs with 8 at. pct Hf addition,[17,23,24] 10 at. pct Hf,[25,26] 15 at. pct Hf,[27–35] and higher Hf additions[36–38] have revealed numerous problems with this system, including thermal cyclic response degradation,[33] brittleness,[38] poor workability,[39] low recoverable and transformation strains,[33] poor thermal and dimensional stability,[10] wide hysteresis,[10] generally poor shape memory response,[33] and nonexistent superelastic behavior.[32] In all these examples, the materials studied were near stoichiometric or Ni lean in composition (containing 50 at. pct or less Ni). More recently, it was realized that it is possible to modify the microstructure of Ni-rich NiTiHf alloys through aging, generating submicron precipitate structures, and stable transformation temperatures.[20] Preliminary results on a Ni-29.7Ti-20Hf (at. pct) alloy indicate that precipitation strengthening also leads to outstanding load-biased shape memory behavior, with little or no irrecoverable strain, and excellent superelastic qualities.[40]

Thus, the objective of the present study was to examine the microstructural mechanisms responsible for the stable high-temperature behavior of a Ni-29.7Ti-20Hf alloy containing coherent nanometer size precipitates. Until now, there were no experimental investigations on the phase-related micromechanical and microstructural behavior of this Ni-rich NiTiHf alloy. *In-situ* neutron diffraction at stress and temperature is a uniquely suited advanced characterization technique that was used to study this alloy at an atomistic level. Compared to conventional X-ray diffraction techniques, neutron diffraction provides greater penetration depths (sampling volumes up to 1 cm^3), representing bulk behavior of polycrystalline samples and avoiding free surface stress effects. Furthermore, in spite of the complicated deformation mechanisms associated with SMAs (*e.g.*, twinning, reorientation, or stress-induced martensite coupled with the possibility for plasticity), it is possible to follow the microstructural changes that occur with stress and temperature, since diffraction patterns are simultaneously recorded. The role of the precipitates during both isothermal and isobaric testing conditions was explored, and the internal strain and texture evolution of martensite and austenite phases were evaluated for this material.

II. EXPERIMENTAL METHODS

A. *Sample Preparation*

A NiTiHf ingot with a nominal composition of 50.3Ni-29.7Ti-20Hf (at. pct) was prepared by vacuum induction melting. The ingot was vacuum homogenized for 72 hours at 1323 K (1050 °C) and furnace cooled followed by hot extrusion (Ext. 124) at 1173 K (900 °C) and an area reduction ratio of 7:1. Cylindrical tensile blanks were removed from the extruded rod and subjected to an aging treatment at 823 K (550 °C) for 3 hours and furnace cooled. This heat treatment was selected after a previous optimization study of different aging temperatures and times, where it was found that these conditions provided the best thermomechanical properties. The cylindrical blanks were then finish machined into dog-bone tensile specimens with final dimensions of 5.08 mm in diameter and 15.24 mm in gage length. After machining, the tensile samples were subjected to one stress-free thermal cycle between room temperature and 573 K (300 °C) in a muffle furnace in air to relieve any residual stresses due to machining and promote a self-accommodated martensite structure. The no-load transformation temperatures, martensite start (M_s), martensite finish (M_f), austenite start (A_s), and austenite finish (A_f), were determined to be 391 K, 382 K, 402 K, and 422 K (118 °C, 109 °C, 129 °C, and 149 °C ± 2 °C), respectively, using the intercept method, as defined in Reference 41.

B. *Experimental Setup and Test Procedures*

In-situ neutron diffraction measurements were performed on the Spectrometer for Materials Research at Temperature and Stress (SMARTS) at the Manuel Lujan Jr. Neutron Scattering Center, LANSCE, at Los Alamos National Laboratory (LANL). Details of the SMARTS engineering instrument are published elsewhere,[42] and only a brief description is presented here. A schematic of the experimental setup with incident and diffracted neutron beams and scattering vectors is shown in Figure 1. The sample was positioned on a horizontal load frame with the loading axis oriented at 45 deg to the incident neutron beam. Two opposing ±90 deg ^{3}He

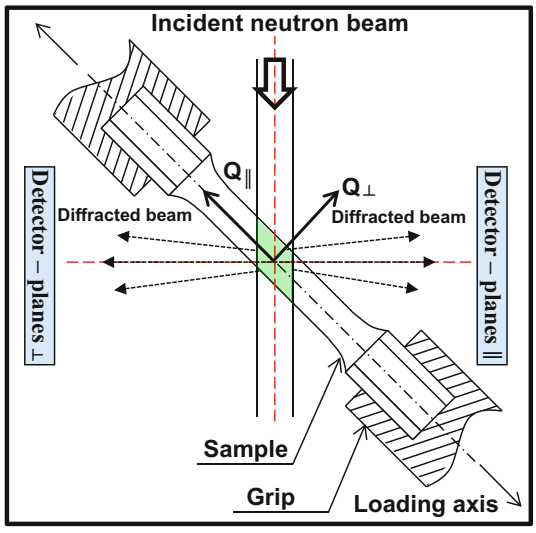

Fig. 1—Schematic of the SMARTS diffractometer experimental setup showing the incident and diffracted beams and scattering vectors (Q). The irradiated volume is shown in green.

tube detector banks recorded scattered neutron data simultaneously with diffraction vectors parallel ($Q_{\parallel}$, –90 deg) and perpendicular ($Q_{\perp}$, +90 deg) to the loading axis. Macroscopic strains were obtained concomitantly while recording neutron data using a high-temperature, 10-mm-gage length extensometer attached to the sample. Heating was controlled using a 5 kW induction heater and a temperature controller interfaced with LabVIEW software from National Instruments, Austin, Texas, while cooling was achieved from natural convection and conduction through the water-cooled grips and pull rods.

To obtain acceptable diffraction intensities, longer count times of about 50 minutes (compared to 30 minutes for binary NiTi) were necessary because of the higher absorption resulting from Hf in the sample. Initially, baseline stress-free diffraction patterns were measured at room temperature and at 573 K (300 °C) for the purpose of (1) determining the count time and (2) examining the initial interplanar spacing and starting texture of both the martensite and austenite phases.

Two types of experiments were carried out in this work; the first experiment consisted of isothermal monotonic loading at room temperature. The applied stress was increased in increments of 25 MPa from 0 to 250 MPa, and in increments of 50 MPa from 250 to 400 MPa at a rate of 30 MPa/min, with diffraction patterns being acquired at each stress increment with hold times of 50 minutes. The second experiment consisted of constant stress (isobaric or load-biased) thermal cycling of the same sample that was used in the first experiment. Without unloading, the 400 MPa stress was held constant and three thermal cycles between room temperature and 573 K (300 °C) were performed with diffraction patterns recorded for each cycle at the two temperature extremes. Finally, the sample was unloaded to 0 MPa followed by two additional stress-free thermal cycles between the same temperatures while recording neutron spectra at room temperature and 573 K (300 °C). The choice of these experimental parameters was based on a condition where this SMA could likely be employed, particularly for high-temperature, high-force actuator applications. At the end of the experiment, the sample was loaded to 800 MPa at room temperature without acquiring neutron data, but the macroscopic stress-strain response was recorded. This data were used to compare the macroscopic responses of the alloy before and after isobaric thermal cycling.

C. *Neutron Diffraction Data Analysis*

Diffraction data were analyzed using two techniques: (1) single-peak fitting and (2) Rietveld refinement. These techniques were successfully applied to the investigation of shape memory NiTi-based alloys.[43–46] From single-peak fits, lattice spacing, integrated intensities, and peak breadths were all resolved using a convolution of Gaussian and Lorentzian functions.[47] The lattice spacing of diffracting grains was used to compute lattice strains from planes parallel and perpendicular to the loading direction using the change in the interplanar spacing, as described elsewhere.[43] In a similar manner, changes in intensities of resolvable diffraction peaks and peak broadening/narrowing were determined. However, the single peak fitting approach is limited to the analysis of single peaks and does not simultaneously consider information from the rest of the diffraction pattern.

On the other hand, Rietveld refinement makes use of the entire diffraction pattern. In this case, lattice parameters were obtained by implementing a least-squares fitting scheme between the entire observed (measured) diffraction pattern and the calculated pattern.[48] The Rietveld refinement code general structure analysis system (GSAS)[49,50] was used to analyze the diffraction patterns and obtain refined crystal structure parameters, lattice strains, phase fractions, and preferred orientation (crystallographic texture). Another advantage of the Rietveld approach is that multiple diffraction peaks, multiple phases, anisotropic effects, and crystallographic orientations were all considered in the fitting process of the entire pattern. Texture, which describes the statistical distribution of the grain orientations in a polycrystalline sample, was examined using an eighth-order spherical harmonic description implemented in the Rietveld refinement code. Texture was also evaluated by looking at the intensities of specific orientations using inverse pole figures (IPFs), which describe the distribution of specific macroscopic directions, *e.g.*, the loading axis, in the coordinate systems of the individual crystallites composing the polycrystal and were obtained by doing a Rietveld refinement on data from one bank of detectors using generic mapping tools.

III. RESULTS

A. *Stress-Free Structure of the Ni-29.7Ti-20Hf Alloy*

Figure 2 shows the refined neutron spectra for the NiTiHf alloy in the stress-free (unloaded) condition. The spectra confirm that the majority phase is B19′ martensite at room temperature and B2 austenite at 573 K (300 °C). These refinements are from reflections with lattice planes parallel to the loading axis that were best fitted using a $P112_1/m$ structure for B19′ martensite and $Pm\bar{3}m$ for B2 austenite. The best-fit lattice parameters, as determined from the Rietveld refinement method, were $a = 3.041$, $b = 4.136$, $c = 4.886$ Å, $\alpha = \gamma = 90$ deg, and $\beta = 104.35$ deg for monoclinic martensite, and $a = 3.086$ Å for cubic austenite.

The profile from the refined martensitic spectrum (Figure 2(a)) was still noisy even after a 50-minute count time, due to the absorption of neutrons by Hf. Even so, it was possible to capture and identify most of the crystallographic peaks. The difference curve plotted below the peak position tick marks shows deviations between the raw neutron data and the Rietveld model. B19′ martensite was the only phase introduced in the refinement scheme, and the observed difference indicates the presence of a secondary phase. This is clearly indicated by the extra peak around a *d*-spacing of 2.16 Å and in other overlapped reflections with the monoclinic matrix that were not captured with the

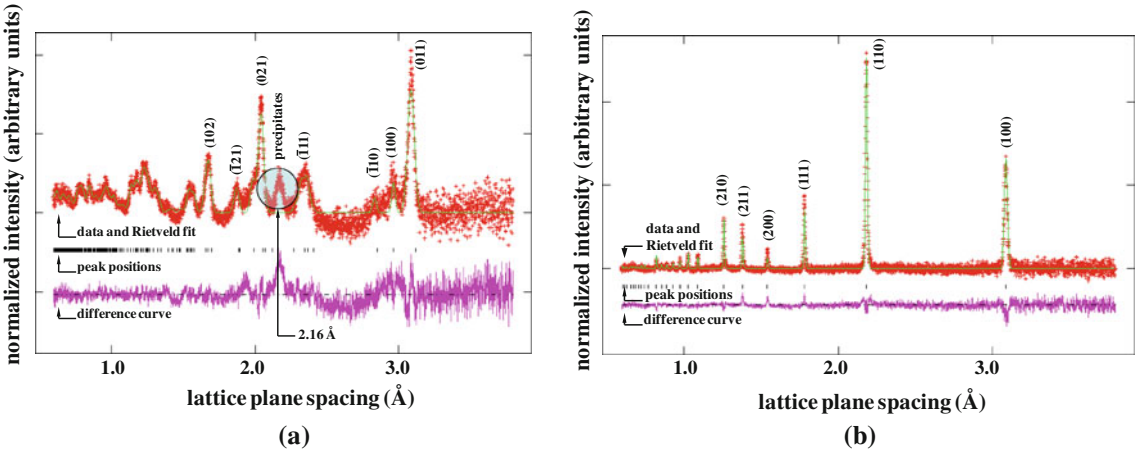

Fig. 2—GSAS Rietveld refinement output for Ni-29.7Ti-20Hf with diffracting lattice planes parallel to the loading axis with no externally applied load: (*a*) monoclinic martensite at 308 K (35 °C) showing a peak attributed to the precipitate phase and (*b*) NiTiHf cubic austenite at 573 K (300 °C). The measured data are indicated by cross marks, and the calculated profile is indicated by the solid line. The tick marks below the profile pattern indicate the reflections. The lower curve is the difference between the measurement and refinement.

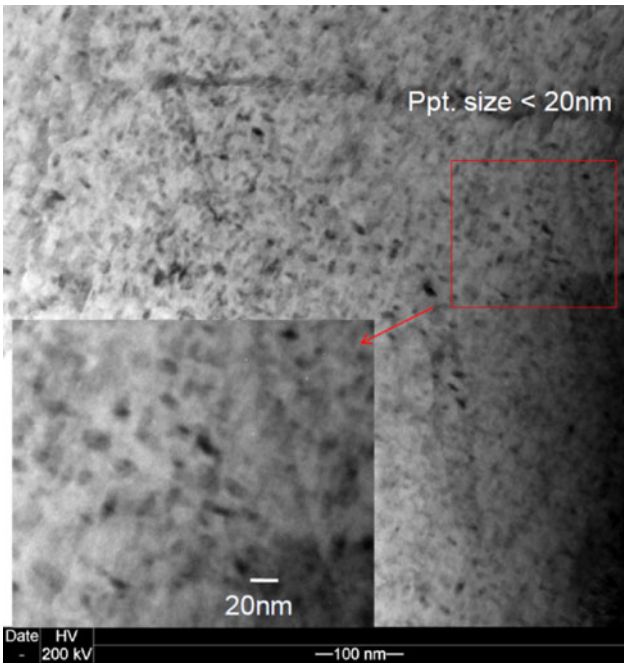

Fig. 3—Bright-field TEM micrograph showing the microstructure of the NiTiHf alloy, consisting of a B19′ monoclinic martensite matrix at room temperature with the inset showing, in more detail, the homogenous distribution of nanometer-sized precipitates.

present single-phase refinement. Transmission electron microscopy (Figure 3) was used to confirm the presence of a high density of fine precipitates (less than 20 nm) in the current alloy resulting from the original 823 K (550 °C), 3-hour aging treatment.

B. *Isothermal Loading in Martensite*

Figures 4(a) and (b) are the room-temperature tensile stress-strain responses of the NiTiHf alloy obtained from extensometry. Figure 4(a) shows the initial loading response, prior to isobaric thermal cycling, and the stresses at which neutron spectra were acquired (indicated by circles). Figure 4(b) shows the loading response of the material (superimposed with the response of Figure 4(a)) after thermal cycling, which consisted of three thermal cycles at 400 MPa followed by an additional two thermal cycles between room temperature and 573 K (300 °C) without load. Thermal cycling appeared to have a negligible effect on the observed stress-strain behavior of the material, as the loading curves up to 400 MPa exhibit nearly identical responses. The sample, initially in a self-accommodated martensitic state, starts deforming elastically before reaching a stress where reorientation/detwinning of the martensite is expected to begin. However, no distinct stress plateau was observed even after loading to 800 MPa (Figure 4(b)), and it was not readily apparent where the onset of inelastic deformation starts for this alloy. Another significant observation is the limited strain (0.7 pct) attained at 400 MPa during isothermal monotonic loading. This deformation strain is a combination of the elastic strain and inelastic martensite variant reorientation/detwinning that is typically expected to be recovered after unloading and heating to the austenite finish temperature. This total macroscopic strain is nearly an order of magnitude lower than that observed for NiTi at comparable stress levels (*e.g.*, ~6 pct strain), where recoverable strains on the order of 5 pct or more are possible through isothermal loading at room temperature followed by thermal recovery.[51]

To investigate the microstructural mechanisms that limit the variant reorientation and detwinning of martensite in this NiTiHf system, neutron diffraction was used. The specimen was loaded under stress control from 0 to 400 MPa with neutron diffraction spectra acquired initially every 25 MPa to capture the start of the stress-strain nonlinearity. Normalized diffraction spectra from lattice planes parallel to the applied stress corresponding to selected stress-strain states are shown in Figure 5. All spectra were normalized to the (120)

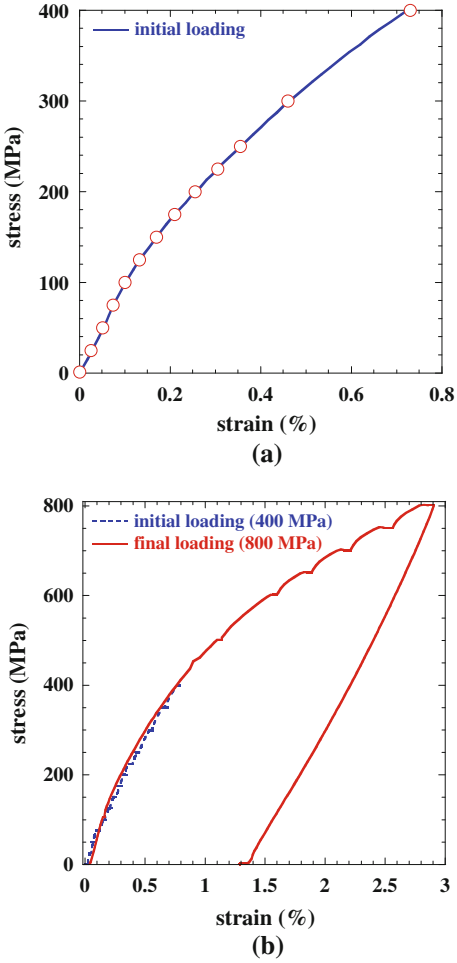

Fig. 4—Tensile stress-strain response of Ni-29.7Ti-20Hf at room temperature (from extensometry): (*a*) Initial loading response showing the onset of nonlinearity and the stresses at which neutron diffraction spectra were acquired; and (*b*) complete loading and unloading curve to 800 MPa, after isobaric thermal cycling, compared to the initial loading response to 400 MPa.

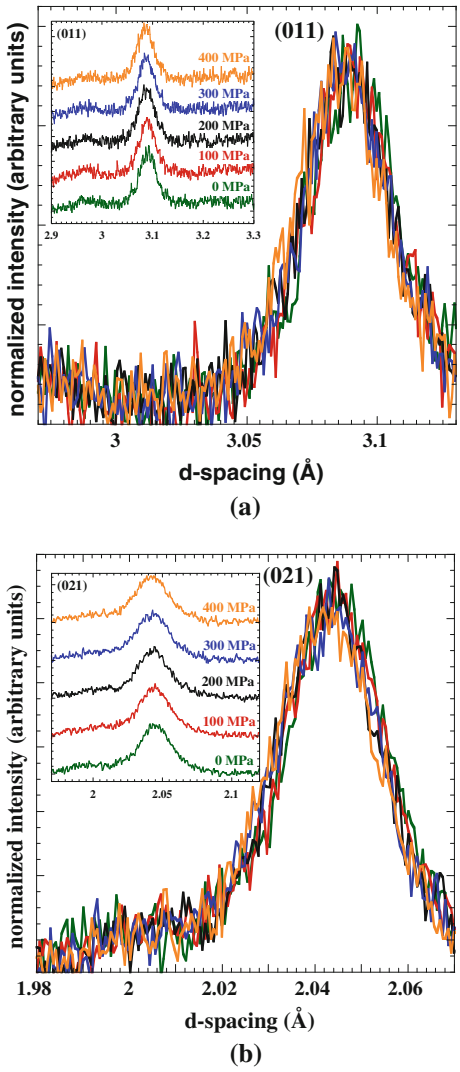

Fig. 5—Sections of normalized neutron diffraction spectra acquired at various stresses during loading to 400 MPa for (*a*) (011) and (*b*) (021) monoclinic crystallographic planes. The reflections are from lattice planes parallel to the loading axis. The insets represent the same spectra offset vertically for clarity.

martensite peak so that they have the same area for all stress increments. For clarity, the same overlay patterns were offset vertically with increasing stress, as shown in the insets of Figure 5. No new peaks and relatively little change in peak intensities were observed as the stress was increased from 0 to 400 MPa. Similar behaviors were apparent using neutron spectra from lattice planes perpendicular to the direction of the applied stress. The absence of a macroscopic stress plateau and limited inelastic strain in Figure 4(a) are consistent with the nearly imperceptible changes in both the (011) and (021) diffraction peaks shown in Figure 5.

Small changes in texture are better detected when the entire spectrum is considered. Therefore, to differentiate any change in texture that might occur during deformation, IPFs were generated using the entire recorded spectra for a given bank of detectors (Figure 6). These IPFs were generated for the minimum unique region for the monoclinic crystal symmetry ($P112_1/m$ structure) in multiples of random distribution. Each IPF is plotted with the corresponding stress at which it was measured and the maximum and minimum pole intensities. Small changes in texture with loading were observed in Figure 6(a) at the (110) and (012) orientations and in Figure 6(b) at the (130) orientation.

Figure 7 shows the elastic lattice strains in the martensite as a function of applied stress obtained from single peak fits for the (011), ($\bar{1}11$), (021), and (030) crystallographic planes. Lattice strains develop in compression or tension depending on whether the diffracting lattice planes are parallel (Poisson strain) or perpendicular to the loading direction. These strains were obtained from shifts in diffraction peaks to lower *d*-spacing for lattice planes parallel to the loading axis due to Poisson contraction, and due to tensile stresses to higher *d*-spacing for lattice planes perpendicular to the loading direction. The strains are the average strain in a subset of all variants with the same crystallographic orientation that contribute to the peak reflection (*i.e.*, all variants with diffracting lattice planes perpendicular to

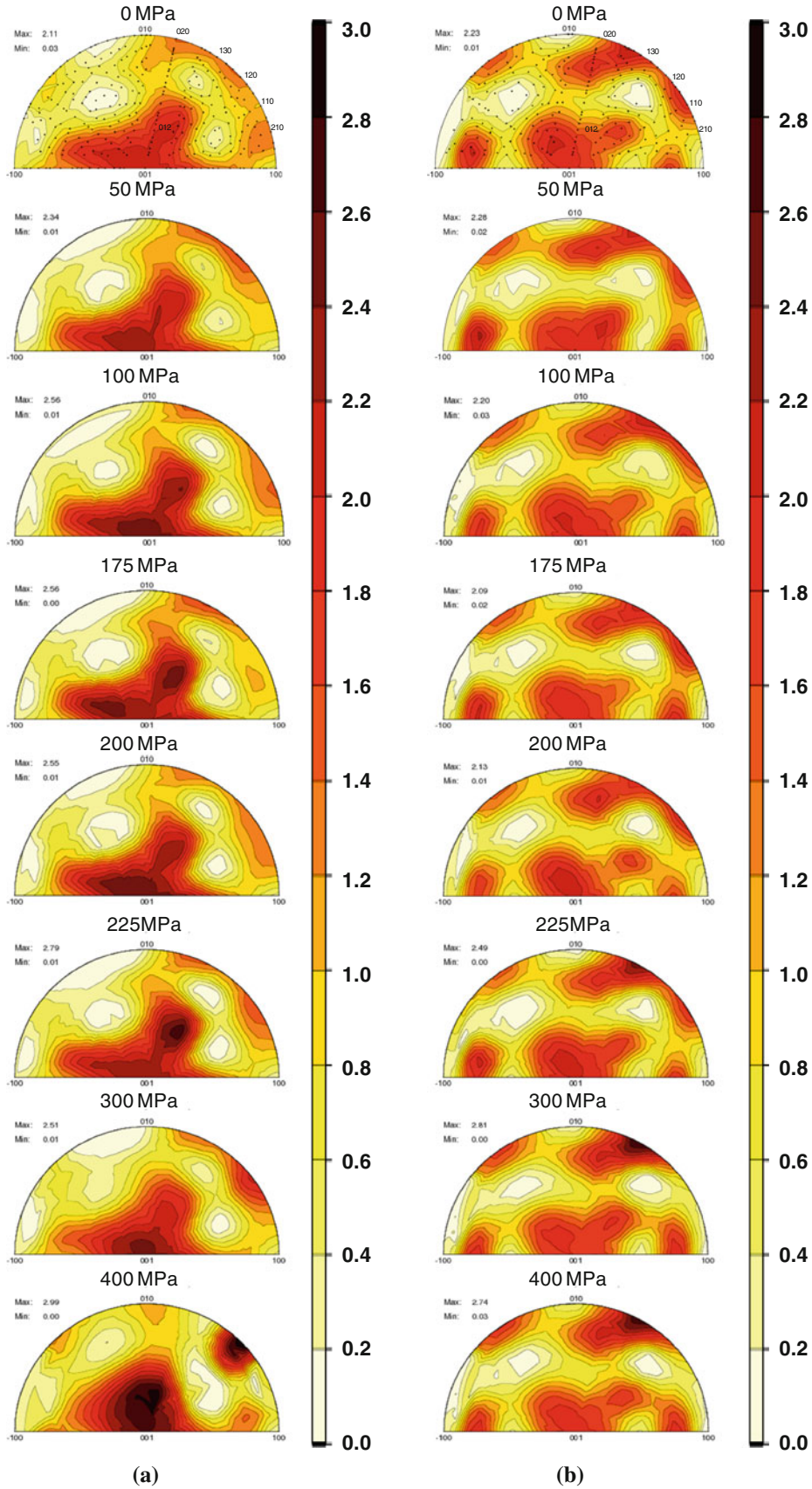

Fig. 6—B19′ martensitic Ni-29.7Ti-20Hf IPFs for diffracting planes (*a*) parallel and (*b*) perpendicular to the loading direction in tension at various stress levels. For a given IPF, the stress state is indicated above the IPF and the corresponding maximum and minimum pole intensities (times random) are at the top left-hand corner.

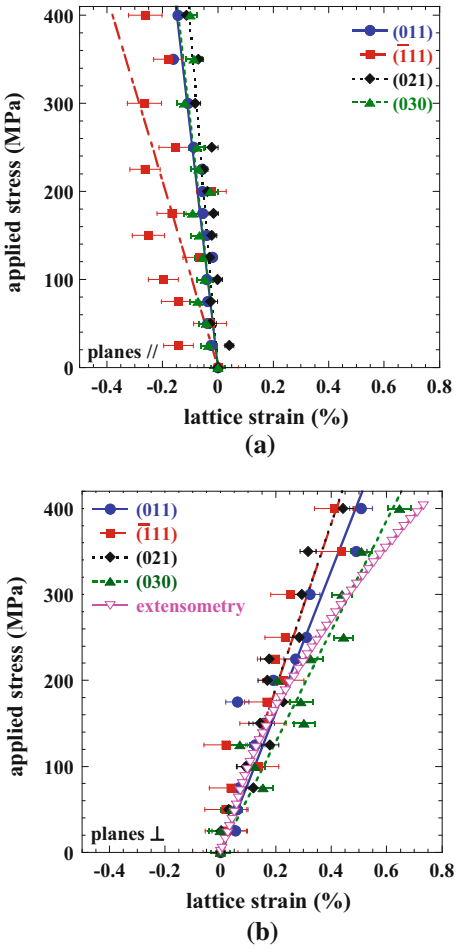

Fig. 7—Lattice strain associated with the (011), (1̄11), (021), and (030) reflections (*a*) parallel and (*b*) perpendicular to the applied loading in tension.

the loading direction). Plane specific elastic moduli in directions normal to given *hkl* planes, E_{hkl}, for stresses up to 100 MPa were determined based on linear fits through the data and were found to be 93, 87, 84, and 64 ± 10 GPa for the (011), (1̄11), (021), and (030) lattice planes, respectively. From extensometry, the elastic modulus was measured for the linear region up to 100 MPa (onset of nonlinearity in lattice strains) and was found to be 87 ± 10 GPa (error from sample to sample variation). Therefore, in this isothermal testing condition, the elastic strain contributions to the overall mechanical response at 400 MPa are about 0.4 pct, where only the remaining 0.3 pct is attributed to the inelastic strains from variant reorientation and detwinning. Plane specific elastic moduli were also observed to exhibit comparatively lower elastic anisotropy than binary NiTi.[51]

C. *Isobaric Strain-Temperature Behavior*

The isobaric strain-temperature response for the NiTiHf alloy is shown in Figure 8. Three thermal cycles are shown, including the first cycle, at a constant stress of 400 MPa between room temperature and 573 K (300 °C). The first heating cycle starts from a strain of

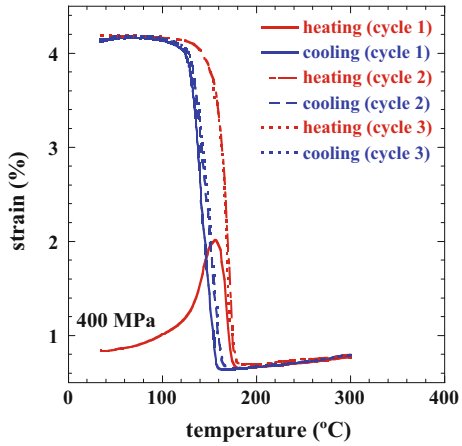

Fig. 8—Strain-temperature response for Ni-29.7Ti-20Hf for the first three thermal cycles at a stress of 400 MPa.

0.8 pct, which was generated from loading to 400 MPa at room temperature (0.1 pct strain higher than the original isothermal loading due to a longer hold time at 400 MPa, while acquiring neutron spectra). As the sample is heated during the first thermal cycle, strain in the uniaxial direction continues to build to about 2 pct and then recovers completely as the sample transforms to B2 austenite. This initial cycle response will be referred to as the transient response in subsequent sections, as this behavior was only observed during the heating portion of the first thermal cycle.

Two important observations can be made from the successive thermal cycles. First, the transformation strains, determined from intercepts of the heating portion of the second and third thermal cycles, were constant at 3.5 pct. This is the available amount of actuation strain associated with a bias stress of 400 MPa. Second, no residual strains (*i.e.*, strain difference between the start and finish of one thermal cycle at room temperature) were observed. No prior training was done to this alloy, and the observed behavior in strain-temperature space was obtained from the three initial cycles of a hot-worked and aged material under stress, demonstrating the inherent dimensional stability of this alloy.

Figure 9 is a compilation of IPFs, acquired at room temperature for the B19′ martensite at the initial no-load condition, the initial isothermal loading to 400 MPa, after the first three load-biased thermal cycles between room temperature and 573 K (300 °C) at 400 MPa, and after the first no-load thermal cycle for both planes parallel and perpendicular to the loading direction. It is clear from the IPFs that the texture evolves during the first thermal cycle and then remains mostly unchanged for subsequent cycles. In particular, the intensities at the (020) orientation (Figure 9(b)) and at the (001) and (120) orientations (Figure 9(a)) increase as the material cycles through the phase transformation for the first time, but do not change significantly for succeeding thermal cycles under the same constant load of 400 MPa. Another important observation is the similarity in texture between the initial IPF and the IPF after the first no-load thermal cycle between room temperature and

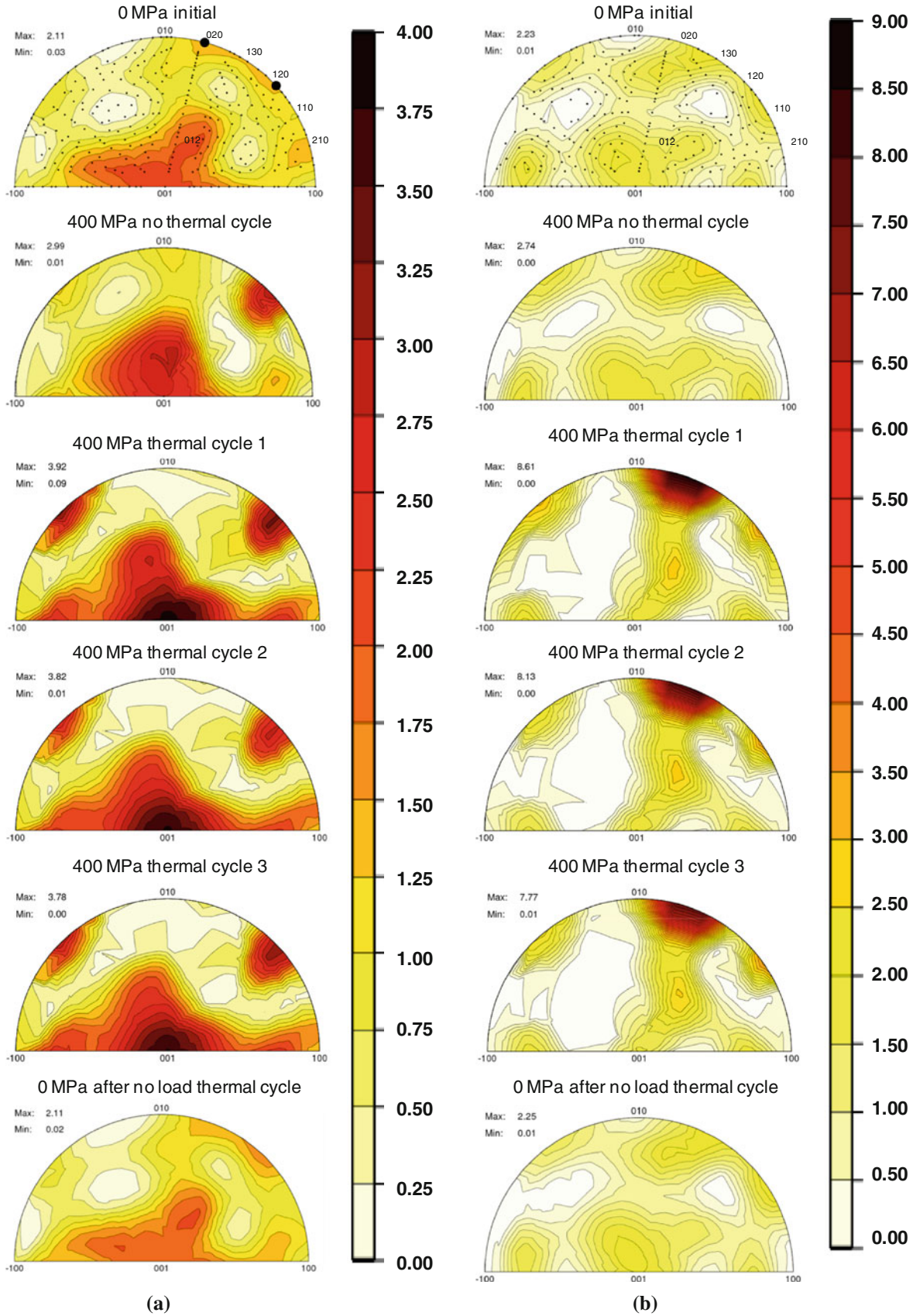

(a) **(b)**

Fig. 9—IPFs for martensitic Ni-29.7Ti-20Hf determined at room temperature from diffracting planes (*a*) parallel and (*b*) perpendicular to the loading direction. From top to bottom, the conditions are (i) as-received material (initial no-load), (ii) after initial load to 400 MPa at room temperature, and after the (iii) first thermal cycle, (iv) second thermal cycle (v) and third thermal cycle between room temperature and 573 K (300 °C) at a stress of 400 MPa. The last IPF (vi) is after the first no-load thermal cycle, post-isobaric thermal cycling.

573 K (300 °C) (top and bottom IPFs). The material is shown to readily revert to the initial self-accommodating texture after the very first no-load thermal cycle. Both sets of data (Figures 9(a) and (b)) show this unique aspect, which further attests to the alloy's inherent stability by demonstrating an insensitivity of the response of the material to prior history.

The observed macroscopic dimensional stability was further investigated from a microstructural perspective by looking at sections of normalized diffraction spectra at 573 K (300 °C), as shown in Figure 10. These spectra correspond to the austenite phase and are from lattice planes parallel to the loading direction. The overlay diffraction patterns were offset vertically with increasing cycle count and are shown in the insets in Figure 10. A significant shift in peak positions to lower *d*-spacing from the no-load condition to the subsequent isobaric cycles was observed, which is due to Poisson strains in planes parallel to the loading direction. The lattice strains from the initial no-load condition to the 400 MPa first cycle were measured for the {100}, {110}, {111}, and {210} crystallographic planes and found to be equal to –0.19 and 0.48 pct for planes parallel and perpendicular (not shown) to the loading axis, respectively. Similar to the isothermal loading in martensite, a sample (not shown here) was loaded in the austenite phase where the plane specific elastic moduli in directions normal to the given *hkl* planes were measured. These moduli were found to be 85, 83, 77, and 80 GPa for the {100}, {110}, {111}, and {210} lattice planes, respectively. From extensometry, the elastic modulus was measured to be 81 GPa. Poisson's ratio was also measured for this austenite phase to be 0.39. From Figure 10, no further shift in *d*-spacing (lattice strain) was seen after the second and third cycles. Note that all lattice planes exhibit nearly the same strain value, which is an indication that the austenite phase is essentially isotropic within experimental error. Texture and peak intensities were also unchanged, both after the initial loading and after thermal cycling. The intensity ratios of {100}/{110} and {100}/{111} planes were found to be 0.62 and 1.38, respectively, for all three cycles. Another important parameter of value from Figure 10 is the peak breadth. Broadening is useful in quantifying the strain anisotropy and dislocation densities. All diffraction patterns for a specific plane were shown to exhibit the same breadth within error. Consequently, the neutron diffraction analyses indicated no evolution or change in the austenite phase with thermal cycling, which is yet another indication of the excellent stability of this alloy.

IV. DISCUSSION

In Sections IV–A through IV–C, the isothermal and isobaric responses of the precipitation-strengthened Ni-29.7Ti-20Hf alloy are discussed with respect to the microstructural observations and micromechanical plane specific strains obtained from the *in-situ* neutron diffraction results.

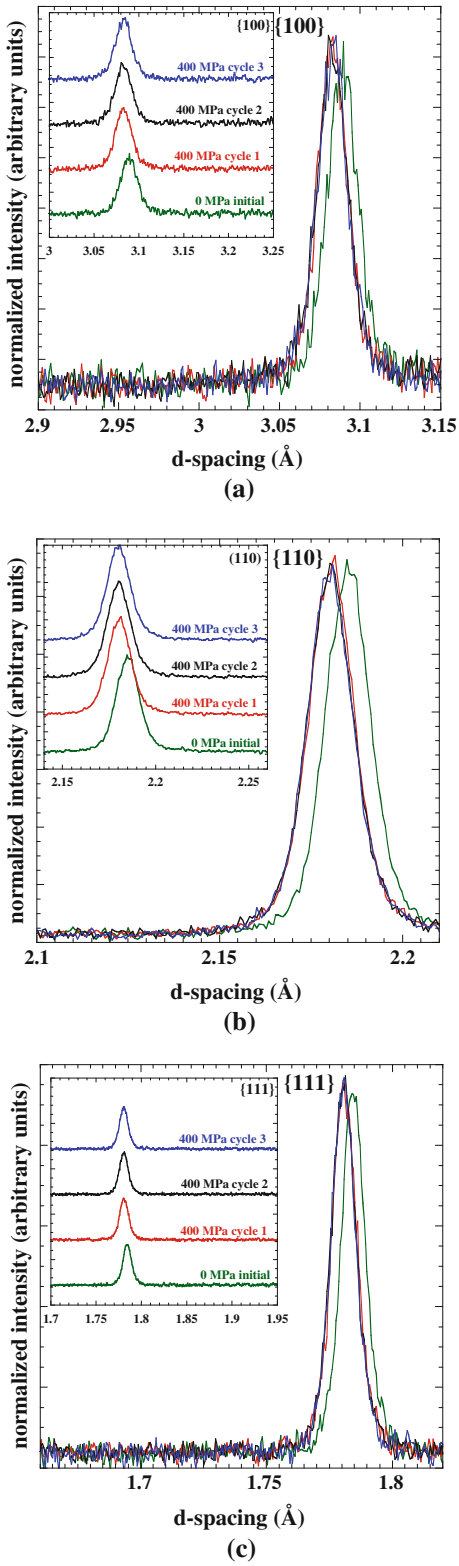

Fig. 10—Sections of the normalized neutron diffraction spectra for Ni-29.7Ti-20Hf austenite phase acquired at 573 K (300 °C) during the first no-load thermal cycle and the first, second, and third isobaric thermal cycles at 400 MPa stress: (*a*) {100}, (*b*) {110}, and (*c*) {111} crystallographic planes. The reflections are from lattice planes parallel to the loading axis.

A. *Initial Ni-29.7Ti-20Hf Microstructure*

The refined B19′ diffraction pattern adequately captures the crystallographic planes that belong to the martensitic phase, but does not include those related to the fine precipitate phase (Figure 2(a)). The presence of a fine precipitate phase was confirmed using transmission electron microscopy (Figure 3), but to date, its structure has not been conclusively identified. It is believed that these fine precipitates are the secondary phase present in the neutron diffraction pattern unaccounted for in the refinement. One of the precipitate phase peaks is clearly shown at a *d*-spacing of 2.16 Å. It is probable that other precipitate peaks are present, but they were not detectable due to convolution with the B19′ monoclinic matrix.

The austenitic diffraction spectrum, taken at 573 K (300 °C), is shown in Figure 2(b). No additional peaks that could be attributed solely to the precipitate phase were observed. This could be due to a close crystallographic relationship and similar crystal orientation as the parent B2 phase, since strains and thermal effects that take place during the martensitic transformation are not large enough to mask the appearance of the precipitate phase in the 573 K (300 °C) diffraction spectrum. This situation would be similar to the case for the fine P_L-phase $Ti_{11}Ni_9Pt_4$ precipitates in Ni-rich NiTiPt.[52,53] In this case, the precipitate has a close relationship to the B2 parent phase due to ordering of Pt on the Ni sublattice. In fact, preliminary results indicate that the fine precipitate phase in the NiTiHf alloy has many similarities to the P_L phase, including a very fine, coherent morphology and a complicated structure with strong relationship to the B2 parent phase.[54] While efforts are continuing to identify the detailed structure of these NiTiHf precipitates, several types of precipitate structures were ruled out for this phase including the P_L phase, the Ni_4Ti_3 phase, and the NiTiHf precipitate phase identified by Han *et al*.[29]

B. *Isothermal Response*

The monotonic room-temperature tension test (Figure 4) served to highlight several characteristics of the stress-strain response of the NiTiHf alloy. The macroscopic B19′ elastic modulus, the onset of detwinning/reorientation, and the elastic and inelastic components of the total isothermal strain were examined. The initial linear elastic portion of the loading curve up to 100 MPa yielded an elastic modulus of 87 ± 10 GPa. The corresponding macroscopic elastic strain (up to 100 MPa) is approximately 0.1 pct. From a macroscopic standpoint, some nonlinearity is noticeable at stresses above 100 MPa, which is considered to be the onset of martensite variant reorientation/detwinning. However, in contrast to other SMA systems (*e.g.*, NiTi[51]), there is no perceptible stress plateau indicative of easy reorientation/detwinning and the inelastic strains generated during deformation were relatively small. Total strains of 0.7 pct at 400 MPa and 2.85 pct at 800 MPa were recorded. This would be the maximum expected strain that could be recovered upon heating to above the austenite finish temperature under stress-free conditions. However, given the fairly large component of elastic strain in these values, the recovered transformation strain would be even smaller. As inelastic deformation starts in the NiTiHf alloy, detwinning of favorably oriented twins does not continue without increasing the externally applied stress. This could be attributed to the interaction of precipitates with the twin and variant boundaries.[55] The mobility of twin and variant boundaries is resisted by the dispersion of fine, coherent precipitates and their associated strain fields, requiring an increasing level of externally applied stress in the system to keep boundaries moving. While these precipitates may pin boundaries, they also act as very efficient obstacles to irreversible plastic deformation. This type of behavior was also observed in Ti-rich NiTiPd alloys containing Ti_2Ni type precipitates[19] and in NiTiPt alloys containing $Ti_{11}Ni_9Pt_4$ type precipitates,[52] where the precipitate phase increased the critical stress for slip in both the low-temperature and high-temperature phases. Evidence for the effectiveness of the precipitate phase in the NiTiHf alloy to resist deformation processes of all kinds can be found in the microstructural observations.

The normalized diffraction intensities (Figure 5) remain mostly unaffected by increasing stress, which is a direct manifestation of limited variant reorientation and detwinning. Consequently, Figure 5 provides indirect microstructural evidence that the martensite variants are pinned by the surrounding precipitates and the associated internal stress fields, resulting in only a small evolution in texture.

For a more sensitive measure of texture, pole intensity changes, which indicate texture evolution, were tracked using IPFs (Figure 6) through appropriate refinement schemes. From the IPFs of diffracting planes parallel to the loading direction (Figure 6(a)), the intensities at the (110) and (012) orientations increase modestly with increasing applied stress at the expense of the (020) and (210) orientations. Likewise, for diffracting planes perpendicular to the loading direction, the intensity at the (130) orientation increases, while the intensity at the (110) orientation decreases. Thus, evidence of martensite reorientation or detwinning was apparent from the IPFs, but was not very pronounced, especially compared to other alloy systems such as binary NiTi.[51] The fact that the texture changes a small amount, however, provides direct experimental evidence of limited variant reorientation and detwinning, leading to the small inelastic strains observed during loading at room temperature.

Elastic strains along various crystallographic planes were assessed for two reasons: (1) to provide insight into the *hkl* elastic moduli and compare them with the macroscopic Young's modulus and (2) to examine the strain anisotropy that arises from the symmetry (or lack of symmetry) of the monoclinic martensite and intergranular interactions. Elastic lattice strains reported here are the average strains measured in all variants homogenously distributed throughout the diffracting volume with their planes oriented perpendicular (plane normals parallel) to the loading direction. Direction-dependent

elastic moduli for directions normal to (011), ($\bar{1}$11), (021), and (030) lattice planes (Figure 7) were determined to be 93, 87, 84, and 64 ± 10 GPa, respectively. Moduli were obtained for stresses up to 100 MPa, since nonlinearities were observed at higher stresses. The anisotropy in these moduli is relatively small (between 64 and 93 GPa) compared to the anisotropy in NiTi, where the moduli for the same four planes were found to vary from 82.3 to 174.5 GPa[51,56] Macroscopically, the elastic modulus was found to be 87 ± 10 GPa, as determined by extensometry. In contrast to the NiTi alloy, where the macroscopic elastic modulus is deflated due to early variant reorientation and detwinning at low stresses, the macroscopic measurement on this alloy can be considered the actual Young's modulus of this material, since variant reorientation and detwinning processes were very limited. Therefore, the measured B19′ Young's modulus can be used for modeling purposes or design without considerable error.

C. *Isobaric Response*

The macroscopic strain-temperature response of the Ni-29.7Ti-20Hf alloy under a constant stress of 400 MPa, shown in Figure 8, provides information on the transient response, transformation temperatures, hysteresis, transformation strains, and unrecoverable (residual) strains. As the sample is heated for the first time at a constant load of 400 MPa, a relatively large (compared to binary NiTi[57]) strain transient develops. Apparently, the additional thermal energy introduced during the initial heating cycle causes further detwinning/reorientation of the martensite phase, which leads to additional inelastic strain in the material. Then, once the austenite start temperature is reached, the original inelastic deformation plus the additional strain that developed during heating start to recover as the material transforms to austenite until all the strain is recovered at the austenite finish temperature. Another possible mechanism that could contribute slightly to this transient response is the change in the material's compliance during heating. This change in compliance was measured for several HTSMA alloys (Figure 20 of Reference 58) using a dynamic technique, where a drop in the Young's modulus was observed with increasing temperatures around the transformation range of each alloy.

During the initial cooling cycle, a relatively large strain (up to 4.1 pct) is generated and this level of strain is reproducibly obtained on the second and third cycles. The enhanced strain during cooling under load is due to the nucleation and growth of preferred martensite variants that favor the applied stress. Evidence for this preferred variant selection under the effect of the applied load was clearly captured by the measured IPFs (Figure 9). During the subsequent heating cycle, all the strain generated during cooling is recovered. The remarkably reproducible strain that is generated each and every cycle (after the initial heating cycle) can be attributed to the presence of the precipitate phase and its effect on this dynamic system. First of all, the precipitate phase effectively resists slip in both the martensite and austenite phases so that plastic deformation, which is an irrecoverable process, does not occur at any point during the transformation process. Also, the strain fields associated with the precipitates act as multiple nucleation sites for martensite. During the forward transformation, martensite nucleates from homogeneously distributed sources throughout the material, essentially in a single burst driven by the strain fields around all the precipitates. Therefore, the transformation is completed over a much narrower temperature range than would be required if only a few fronts were nucleated and had to propagate through a larger volume of material, storing additional elastic strain energy. The disadvantage to nucleation of martensite in this manner is that transformation strains will tend to be smaller than in precipitate-free material because of fewer variant interactions. However, in practice, the advantage of enhanced strain expected of single-phase material is usually offset by the early onset of plastic deformation and a lack of dimensional stability.

The transformation temperatures at this selected load were also assessed. At 400 MPa, the martensite start, martensite finish, austenite start, and austenite finish temperatures were determined to be 436 K (163 °C), 404 K (131 °C), 431 K (158 °C), and 451 K ± 2 K (178 °C ± 2 °C), respectively. These temperatures were found to be different from what is reported in Reference 40, where the corresponding transformation temperatures were determined to be 452 K, 432 K, 456 K, and 473 K (179 °C, 159 °C, 183 °C, and 200 °C), respectively. This approximately 295 K (22 °C) difference in transformation temperatures is likely due to the manner in which the temperature was measured. In Reference 40, the temperature was measured using a thermocouple spot welded directly to the specimen gage section, while in this study, the temperature was measured using a thermocouple tied to the specimen, which would tend to underestimate the actual temperature of the material. Heat-to-heat compositional variation could also play a role in the observed discrepancy.

Hysteresis is another important parameter, particularly for active control and high frequency response applications. Large hystereses on the order of 313 K to 353 K (40 °C to 80 °C) were observed in Ti-rich or near-stoichiometric NiTiHf alloys containing 15 to 20 pct Hf.[59–61] In this work, a relatively small hysteresis in the order of 293 K to 298 K (20 °C to 25 °C) was obtained, which is comparable to that reported previously.[40] The decreased hysteresis is attributed to the effect of the precipitates to nucleate the transformation from sources homogeneously distributed throughout the material, resulting in reduced overall movement of transformation fronts rather than having to pass a few transformation fronts through larger volumes in the material. The consequence of this reduced movement of the fronts or interfaces is reduced frictional resistance, energy dissipation, and hysteresis.

Transformation strains during 400 MPa load-biased thermal cycling were determined to be 3.5 pct and are repeatable from cycle to cycle through the third cycle shown in Figure 8. This strain is associated with the orientation of selected martensite variants. Preferred variant selection under load, indicated by the high

intensity at the (020) orientation in Figure 9(b), is identically promoted in each cycle by the applied load and magnified by the stress concentration due to the presence of the precipitates that, in turn, act as homogeneous sources for the nucleation of martensite throughout the material. This is in contrast to inhomogeneous nucleation of martensite and the subsequent growth of a few phase fronts, as occurs in single-phase alloys. As a result, cycling under load leads to a near identical transformation strain of 3.5 pct for each cycle. This transformation strain value was used to calculate the work output of the SMA, an important property in actuator applications, which was determined to be 14 J cm^{-3}. It was shown in Reference 40 that the work output in this alloy is at least 18.7 J cm^{-3} at a stress level of 500 MPa. Hence, this precipitation-strengthened alloy is a promising replacement for conventional actuation systems.

Stability was also examined by measuring the amount of irrecoverable strain that developed during thermal cycling by looking at the difference in strain at room temperature after each thermal cycle. At the end of the second cycle, the unrecoverable strain was about 10^{-3} pct and was negligibly changed in the subsequent third cycle. This is an indication of nearly perfect dimensional stability without any prior training of the material. This improved stability is promoted by the existence of the precipitates, which has at least two major effects on the overall microstructure. The first is providing resistance to permanent deformation mechanisms such as slip, as was discussed in preceding sections. For instance, the applied 400 MPa stress is below the stress at which slip would be activated over twinning. The second effect is the prevention of retained martensite above the austenite finish temperature, which was shown to be responsible for a major component of total accumulated strain after cycling of a NiTiPd HTSMA.[62] This latter effect is demonstrated in Figure 10, which shows that there is no texture evolution in the austenite phase and no martensite peaks appear in the spectra recorded at 573 K (300 °C) during thermal cycling.

This unchanging austenitic texture is also an indication that no new or additional deformation mechanisms ensue from thermal cycling under a 400 MPa bias stress. The initial shift in position in all three peaks is due to the elastic lattice strains found to be –0.19 pct as a result of the 400 MPa stress. For the subsequent cycles, no additional shift is observed in the recorded reflections. These equivalent lattice strains for the subsequent cycles are consistent with the lack of macroscopic residual strain development during load-biased thermal cycling (Figure 8). Moreover, all diffraction patterns are shown to exhibit the same breadth. Hence, the transformation to the parent austenite phase is identically recovered after each cycle with no change in texture, no retained martensite, and no evidence of any plastic or other inelastic deformation mechanisms, consistent with the thermomechanical test results and the lack of any residual strain after load-biased thermal cycling.

From the no load thermal cycles performed after the load-biased tests, the measured texture was found to be nearly identical to the initial starting texture. This ability to revert back to the initial self-accommodated state after only one no-load thermal cycle demonstrates essentially history-independent behavior for this alloy, which is quite rare in any SMA system. This complete reversion to its original self-accommodated state after thermomechanical testing is also demonstrated by reloading the sample at room temperature, where its tensile behavior after all these thermomechanical cycles is identical to its original state (Figure 4(b)). Since the material easily reverts back to a self-accommodated texture when the load is released, it can be optimized or trained under new conditions without being affected by loading path history. For other alloys with no precipitates, for example, 55NiTi or NiTiPd alloys, training using this same isobaric cycling method will require a large number of cycles as the material tends to evolve or de-evolve to its saturated state.[8,63] The current NiTiHf SMA only requires a few thermal cycles under a particular (stress-temperature) condition for it to be fully trained. Therefore, training to optimum behavior is actually much easier without costly and time-consuming training procedures.

V. CONCLUSIONS

The study of uniaxial tension experiments, both in isothermal and isobaric testing modes, was presented for a Ni-rich NiTiHf alloy. The stability of this HTSMA was investigated macroscopically through extensometry measurements and concurrently at the microscopic level with *in-situ* neutron diffraction at stress and temperature. The stability of the alloy in terms of the observed strain characteristics was elucidated by examining the crystal structure, micromechanics, and microstructure evolution resulting in the following conclusions.

1. Neutron and electron diffraction confirmed the formation of fine, nanometer size, coherent precipitates through careful stoichiometry control and aging. This precipitate phase is believed to be the stabilizing factor in this NiTiHf alloy.
2. During isothermal deformation, restricted detwinning and low isothermal strains were consistent with limited martensite texture changes, as observed in diffraction spectra and IPFs. Limited detwinning was attributed to the pinning of twin and variant boundaries by the dispersion of fine precipitates.
3. Average monoclinic lattice elastic strain limits were found to be of the order of 0.1 pct strain, and the corresponding plane specific elastic moduli for directions normal to (011), ($\bar{1}$11), (021), and (030) lattice planes were 93, 87, 84, and 64 ± 10 GPa, respectively, and exhibited relatively small anisotropy compared to binary NiTi.
4. The observed transient strain response during the first load-biased thermal cycle was relatively large compared to binary NiTi. This behavior is believed to result from (1) additional detwinning and reorientation as the mobility of twin/variant boundaries increases with temperature and (2) changes in the

material's compliance with the additional thermal energy.

5. Relatively narrow hysteresis, on the order of 293 K to 298 K (20 °C to 25 °C), bodes well for use of this alloy in active and precise control applications. This reduced hysteresis, when compared to other SMAs, is a result of the role of the precipitates to nucleate the transformation homogeneously throughout the material over a very narrow temperature window.
6. Repeatable high transformation strains (3.5 pct at 400 MPa, 14 J cm^{-3} work output) and insignificant unrecoverable strains ($<10^{-3}$ pct) during isobaric thermal cycling make this alloy a good candidate for actuator applications at high temperatures (above 373 K (100 °C)).
7. Excellent shape memory behavior with nearly 100 pct shape recovery in the initial cycles eliminates the need for costly and time-consuming training.
8. The ability of this alloy to revert readily to the initial self-accommodating structure after only one no-load thermal cycle indicates history-independent behavior and further explains the excellent stability in this Ni-rich NiTiHf HTSMA.

ACKNOWLEDGMENTS

Funding from the NASA Fundamental Aeronautics Program, Supersonics Project (Grant No. NNX08A-B51A), is gratefully acknowledged. The authors thank D.W. Brown, B. Clausen, and T. Sisneros (LANL) and D. Gaydosh, G. Bigelow, and A. Garg (NASA GRC) for technical support and helpful discussions. D.E. Nicholson's help in performing the neutron diffraction experiments is gratefully acknowledged. This work benefited from the use of the Lujan Neutron Scattering Center, LANSCE, which is funded by the Office of Basic Energy Sciences, United States Department of Energy. LANL is operated by Los Alamos National Security LLC under the United States Department of Energy Contract No. DE-AC52-06NA25396.

REFERENCES

1. S. Hirose, K. Ikuta, and Y. Umetani: *Adv. Robot*., 1989, vol. 3, pp. 3–16.
2. C. Mavroidis: *Res. Nondestr. Eval*., 2002, vol. 14, pp. 1–32.
3. D.J. Hartl, D.C. Lagoudas, F.T. Calkins, and J.H. Mabe: *Smart Mater. Struct*., 2010, vol. 19, p. 015020.
4. D.J. Hartl, D.C. Lagoudas, F.T. Calkins, and J.H. Mabe: *Smart Mater. Struct*., 2010, vol. 19, p. 015021.
5. D. Stoeckel: *Mater. Des*., 1990, vol. 11, pp. 302–07.
6. Ravi Vaidyanathan, H.J. Chiel, and R.D. Quinn: *Rob. Autom. Syst*., 2000, vol. 30, pp. 103–13.
7. K. Otsuka and C.M. Wayman: *Shape Memory Materials*, Cambridge University Press, Cambridge, U.K., 1999.
8. G.S. Bigelow, S.A. Padula II, A. Garg, D.J. Gaydosh, and R.D. Noebe: *Metall. Mater. Trans. A*, 2010, vol. 41A, pp. 3065–79.
9. C. Grossmann, J. Frenzel, V. Sampath, T. Depka, and G. Eggeler: *Metall. Mater. Trans. A*, 2010, vol. 40A, pp. 2530–44.
10. J. Ma, I. Karaman, and R.D. Noebe: *Int. Mater. Rev*., 2010, vol. 55, pp. 257–315.
11. G.S. Bigelow, S.A. Padula II, A. Garg, and R.D. Noebe: *SPIE*, Bellingham, WA, 2007, vol. 6526, pp. 65262B-1–65262B-12.
12. K.C. Atli, I. Karaman, R.D. Noebe, A. Garg, Y.I. Chumlyakov, and I.V. Kireeva: *Metall. Mater. Trans. A*, 2010, vol. 41A, pp. 2485–97.
13. G.S. Firstov, J. Van Humbeeck, and Y.N. Koval: *Mater. Sci. Eng. A*, 2004, vol. 378, pp. 2–10.
14. K. Otsuka and X. Ren: *Intermetallics*, 1999, vol. 7, pp. 511–28.
15. K.C. Atli, I. Karaman, R.D. Noebe, and H.J. Maier: *Scripta Mater*., 2011, vol. 64, pp. 315–18.
16. B. Kockar, K.C. Atli, J. Ma, M. Haouaoui, I. Karaman, M. Nagasako, and R. Kainuma: *Acta Mater*., 2010, vol. 58, pp. 6411–20.
17. B. Kockar, I. Karaman, J.I. Kim, and Y. Chumlyakov: *Scripta Mater*., 2006, vol. 54, pp. 2203–08.
18. J. Ma, I. Karaman, B. Kockar, H.J. Maier, and Y.I. Chumlyakov: *Mater. Sci. Eng. A,* 2011, vol. 528, pp. 7628–35.
19. S. Shimizu, Y. Xu, E. Okunishi, S. Tanaka, K. Otsuka, and K. Mitose: *Mater. Lett*., 1998, vol. 34, pp. 23–29.
20. X.L. Meng, W. Cai, Y.D. Fu, Q.F. Li, J.X. Zhang, and L.C. Zhao: *Intermetallics*, 2008, vol. 16, pp. 698–705.
21. D.Y. Cong, S. Wang, Y.D. Wang, Y. Ren, L. Zuo, and C. Esling: *Mater. Sci. Eng. A*, 2008, vol. 473, pp. 213–18.
22. E. Panchenko, Y. Chumlyakov, H.J. Maier, E. Timofeeva, and I. Karaman: *Intermetallics*, 2010, vol. 18, pp. 2458–63.
23. F. Dalle, E. Perrin, P. Vermaut, M. Masse, and R. Portier: *Acta Mater*., 2002, vol. 50, pp. 3557–65.
24. P.L. Potapov, A.V. Shelyakov, A.A. Gulyaev, E.L. Svistunov, N.M. Matveeva, and D. Hodgson: *Mater. Lett*., 1997, vol. 32, pp. 247–50.
25. P.E. Thoma and J.J. Boehm: *Mater. Sci. Eng. A*, 1999, vols. 273–275, pp. 385–89.
26. S. Besseghini, E. Villa, and A. Tuissi: *Mater. Sci. Eng. A*, 1999, vols. 273–275, pp. 390–94.
27. S. Han, W. Zou, S. Jin, Z. Zhang, and D. Yang: *Scripta Metall. Mater*., 1995, vol. 32, pp. 1441–46.
28. X.D. Han, R. Wang, Z. Zhang, and D.Z. Yang: *Mater. Lett*., 1997, vol. 30, pp. 23–28.
29. X.D. Han, R. Wang, Z. Zhang, and D.Z. Yang: *Acta Mater*., 1998, vol. 46, pp. 273–81.
30. X.D. Han, W.H. Zou, R. Wang, Z. Zhang, and D.Z. Yang: *Acta Mater*., 1996, vol. 44, pp. 3711–21.
31. X.L. Meng, W. Cai, Y.F. Zheng, Y.B. Rao, and L.C. Zhao: *Mater. Lett*., 2003, vol. 57, pp. 4206–11.
32. X.L. Meng, W. Cai, Y.F. Zheng, Y.X. Tong, L.C. Zhao, and L.M. Zhou: *Mater. Lett*., 2002, vol. 55, pp. 111–15.
33. X.L. Meng, Y.F. Zheng, Z. Wang, and L.C. Zhao: *Mater. Lett*., 2000, vol. 45, pp. 128–32.
34. Y.Q. Wang, Y.F. Zheng, W. Cai, and L.C. Zhao: *Scripta Mater*., 1999, vol. 40, pp. 1327–31.
35. Y. Tong, F. Chen, B. Tian, L. Li, and Y. Zheng: *Mater. Lett*., 2009, vol. 63, pp. 1869–71.
36. R. Santamarta, C. Seguí, J. Pons, and E. Cesari: *Scripta Mater*., 1999, vol. 41, pp. 867–72.
37. M. Zarinejad, Y. Liu, and T.J. White: *Intermetallics*, 2008, vol. 16, pp. 876–83.
38. M. Liu, X.M. Zhang, Y.Y. Li, J.Z. Chen, and M.J. Tu: *J. Alloys Compd*., 2002, vol. 334, pp. 147–53.
39. C.C. Wojcik: *J. Mater. Eng. Perf*., 2009, vol. 18, pp. 511–16.
40. G.S. Bigelow, A. Garg, S.A. Padula II, D.J. Gaydosh, and R.D. Noebe: *Scripta Mater*., 2011, vol. 64, pp. 725–28.
41. ASTM Standard F2082–06, "Standard Test Method for Determination of Transformation Temperature of Nickel-Titanium Shape Memory Alloys by Bend and Free Recovery," ASTM International, West Conshohocken, PA, 2010, www.astm.org.
42. M.A.M. Bourke, D.C. Dunand, and E. Ustundag: *Appl. Phys. A*, 2002, vol. 74, pp. s1707–09.
43. S. Qiu, V. Krishann, S.A. Padula II, R.D. Noebe, B. Clausen, and R. Vaidyanathan: *Appl. Phys. Lett*., 2009, vol. 95, pp. 141906-1–141906-3.
44. C.R. Rathod, B. Clausen, M.A.M. Bourke, and R. Vaidyanathan: *Appl. Phys. Lett*., 2006, vol. 88, pp. 201919-1–201919-3.
45. R. Vaidyanathan, M.A.M. Bourke, and D.C. Dunand: *J. Appl. Phys*., 1999, vol. 86, pp. 3020–29.
46. V.B. Krishnan, R.M. Manjeri, B. Clausen, D.W. Brown, and R. Vaidyanathan: *Mater. Sci. Eng. A*, 2008, vols. 481–482, pp. 3–10.
47. R.B. Von Dreele: *J. Appl. Crystallogr*., 1997, vol. 30, pp. 517–25.

48. M.R. Daymond, M.A.M. Bourke, R.B. Von Dreele, B. Clausen, and T. Lorentzen: *J. Appl. Phys.*, 1997, vol. 82, pp. 1554–62.
49. A.C. Larson and R.B. Von Dreele: "General Structure Analysis System (GSAS)," Los Alamos National Laboratory Report No. LAUR 86-748, Los Alamos, NM, 2004.
50. R.B. Von Dreele, J.D. Jorgensen, and C.G. Windsor: *J. Appl. Crystallogr.*, 1982, vol. 15, pp. 581–89.
51. S. Qiu, B. Clausen, S.A. Padula II, R.D. Noebe, D.J. Gaydosh, and R. Vaidyanathan: *Acta Mater.*, 2011, vol. 59, pp. 4660–73.
52. L. Kovarik, F. Yang, R.D. Noebe, and M.J. Mills: *Microsc. Microanal.*, 2009, vol. 15, pp. 1402–03.
53. L. Kovarik, F. Yang, A. Garg, D. Diercks, M. Kaufman, R.D. Noebe, and M.J. Mills: *Acta Mater.*, 2010, vol. 58, pp. 4660–73.
54. T. Sasaki: University of Alabama, Tuscaloosa, AL, personal communication, 2010.
55. S. Banerjee and J. Mukhopadhyay: *Phase Transformations—Examples from Titanium and Zirconium Alloys*, Pergamon, Oxford, United Kingdom, 2007.
56. M.F.-X. Wagner and W. Windl: *Acta Mater.*, 2008, vol. 56, pp. 6232–45.
57. S.A. Padula II, S. Qiu, D.J. Gaydosh, R.D. Noebe, G.S. Bigelow, A. Garg, and R. Vaidyanathan: "Effect of Upper-Cycle Temperature on the Load-Biased, Strain-Temperature Response of NiTi", NASA/TM–2011-217408, NASA, Washington, DC, 2011.
58. A. Stebner, S.A. Padula II, R. Noebe, B. Lerch, and D. Quinn: *J. Intell. Mater. Syst. Struct.*, 2009, vol. 20, pp. 2107–26.
59. D.R. Angst, P.E. Thoma, and M.Y. Kao: *J. Phys. IV*, 1995, vol. 5, pp. C8–747.
60. X.L. Meng, Y.F. Zheng, Z. Wang, and L.C. Zhao: *Scripta Mater.*, 2000, vol. 42, pp. 341–48.
61. P. Olier, J.C. Brachet, J.L. Bechade, C. Foucher, and G. Guenin: *J. Phys. IV*, 1995, vol. 5, C8–741.
62. J.A. Monroe, I. Karaman, D.C. Lagoudas, G.S. Bigelow, R.D. Noebe, and S.A. Padula II: *Scripta Mater.*, 2011, vol. 65, pp. 123–26.
63. K. Atli: Ph.D. Dissertation, Texas A&M University, College Station, TX, Aug. 2011.